

Marshall University

Marshall Digital Scholar

Theses, Dissertations and Capstones

2019

Hybrid Excitations in Organic-Semiconductor Materials

David W. Facemyer

Follow this and additional works at: <https://mds.marshall.edu/etd>



Part of the [Condensed Matter Physics Commons](#), and the [Quantum Physics Commons](#)

HYBRID EXCITATIONS IN ORGANIC-SEMICONDUCTOR MATERIALS

A thesis submitted to
the Graduate College of
Marshall University
In partial fulfillment of
the requirements for the degree of
Master of Science

in

Physics

by

David W. Facemyer

Approved by

Dr. Huong Nguyen, Committee Chairperson

Dr. Thomas Wilson

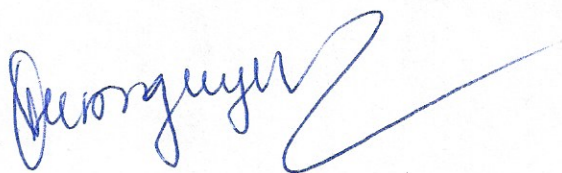
Dr. Judy Fan

Marshall University

December 2019

APPROVAL OF THESIS

We, the faculty supervising the work of David W. Facemyer, affirm that the thesis, HYBRID EXCITATIONS IN ORGANIC-SEMICONDUCTOR MATERIALS, meets the high academic standards for original scholarship and creative work established by the Department of Physics and the College of Science. This work also conforms to the editorial standards of our discipline and the Graduate College of Marshall University. With our signatures, we approve the manuscript for publication.

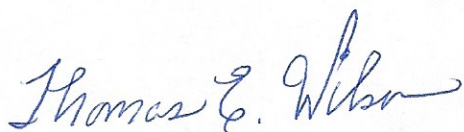


Dr. Huong Nguyen, Department of Physics

Committee Chairperson

11/13/2019

Date

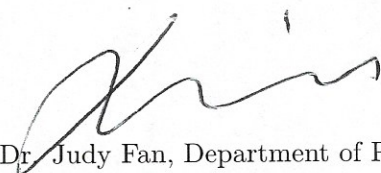


Dr. Thomas Wilson, Department of Physics

Committee Member

11/13/19

Date



Dr. Judy Fan, Department of Physics

Committee Member

11/13/19

Date

© 2019
David W. Facemyer
ALL RIGHTS RESERVED

ACKNOWLEDGEMENTS

I want to first mention my family and friends, without whom crazy ideas stay ideas. Many hours were spent discussing dreams and convictions, and mine are stronger because of you. Next, I would like to extend my debt of gratitude to Dr. Que Huong Nguyen, my advisor and mentor for far longer than she had agreed. Thank you for seeing something in me that I find difficult to acknowledge myself. You always did your best to animate the lifeless equations. To my wife, Amy. You have stood by me through it all, *it was the best of times and the worst of times*, and your support would take volumes to detail. You pushed me through the muck and mire of research; you motivated me to press on. To my son, Isaac. Watching your curiosity grow with every question I tried to answer is a priceless treasure that I will always hold tightly in my heart. Never stop looking at the stars and wondering *how* and *why*. Finally, I give immeasurable thanks to the architect of it all. Your creation has inspired me from the time I first opened my eyes and will continue to inspire me until the time I finally close them. Our physics are the words you used to speak the universe into existence, and I want to know it all.

TABLE OF CONTENTS

Approval of Thesis	ii
List of Figures	vi
Abstract	viii
Chapter 1 Introduction.....	1
1.1 Excitations as Quasiparticles	2
1.2 Geometry and its Influence	2
Chapter 2 Exciton Hybridization	4
2.1 Coupled Two-Oscillator Dispersion	4
2.2 Wannier-Frenkel Exciton Hybridization.....	6
2.3 Numerical Analysis of Engelmann's, et al. Hybridization Parameter.....	9
2.4 Organic-Inorganic Exciton Optical Nonlinearity	11
Chapter 3 Hybrid Exciton-Polariton	13
3.1 Coupled Three-Oscillator Dispersion	13
3.2 Numerical Analysis of the Hybrid Polariton	16
Chapter 4 Stark Effect on Hybrid Excitons	18
4.1 The Electron and Hole in a Quantum Dot of known Radius	18
4.2 Stark Effect on the Hybrid Exciton	19
Chapter 5 Conclusion	22
References	24
Appendix A Approval Letter.....	25
Appendix B Sample Calculation for A-Coefficient in Stark Effect	26

LIST OF FIGURES

Figure 1	Two examples of different heterostructure geometries.	3
Figure 2	Example of a hybrid exciton dispersion and branch mixing. The red and black curves reflect the red and black dotted curves of the pure states on the dispersion graph, respectively.	5
Figure 3	An example of the hybrid exciton dispersion curve shifting in response to a change in the detuning of the system by 50meV.	6
Figure 4	The dipole moments of excitons in a quantum dot with organic shell.	7
Figure 5	Calculated Bohr radii and dielectric constants for various common, inorganic semiconductor materials with logarithmic curve-fitting.	9
Figure 6	Density plots for the hybridization parameter dependent on the semiconductor exciton Bohr radius, the core-shell filling factor, and the ratio of inorganic to organic dielectric constants.	10
Figure 7	A sliced density plot that illustrates the relatively negligible influence that the dielectric ratio has on the hybridization parameter.	11
Figure 8	Surface plots for three different core-exciton Bohr radii to illustrate the significance of the core-shell interface <i>roughness</i>	12
Figure 9	A log-plot for the rough orders of magnitude of third-order nonlinearity ratios dependent on the CSNP filling factor. Each curve is a different average shell thickness to organic lattice constant ratio. b) is the desired filling factor region.	12
Figure 10	Relationship between the angle of incidence θ and the polariton energy.	15
Figure 11	Relationship between the angle of incidence θ and the branch mixing coefficients.	16

Figure 12	The dispersion and middle branch mixing curves for the hybrid polariton in the case of a CdSe core. a) and b) illustrate the case when the hybridization parameter is 1 meV, while c) and d) depict the case when the hybridization parameter is 30 meV.	17
Figure 13	A schematic showing the predicted splitting of the two Wannier-Mott exciton states by respective factors due to an applied electric field.	21

ABSTRACT

It has been suggested theoretically and realized experimentally that combining organic material and inorganic semiconductors in one heterostructure would result in resonant interactions between the Frenkel excitons in the organic material and the Wannier-Mott excitons in the semiconductors, leading to the formation of an exciton hybridization state. The new materials, possessing the complimentary characteristics of both exciton types, such as large exciton radius, enormous oscillator strength and room-temperature operation properties, would enhance optical nonlinearities and promise to have useful applications in both the field of Bose-Einstein condensation of polaritons and polariton lasers. In this work, we consider a strong coupling of the hybrid excitons and photons near excitonic resonance analytically with the purpose of determining the electronic structure, energy, and dispersion relation of the hybrid exciton-polariton. We study different confinement parameters for various nano-scale heterostructures, and in doing so, we discuss the conditions necessary for their formation. Our *ab initio* approach moves us a step closer to realizing new, novel optoelectrical materials that exhibit the strengths of each constituent.

CHAPTER 1

INTRODUCTION

Recent development of technology opens a new opportunity of incorporating organic and inorganic-semiconductor materials in combined low-dimensional heterostructure systems.

Quantum size effects of the motion of electrons and holes in low-dimensional heterostructures lead to many interesting optical and structural phenomena.

In inorganic-semiconductors, Wannier-Mott excitons have large exciton radii and weak oscillator strengths, large exciton-exciton interaction and low saturation exciton density. In organic materials, by contrast, small-radius Frenkel excitons have comparatively large oscillator strengths, small exciton-exciton interaction and very large saturation density. When a semiconductor is placed next to an organic material in a combined organic-inorganic heterostructure configuration, the Wannier exciton and the Frenkel exciton interact with each other and a special kind of hybridization state, the hybrid exciton, is formed at a junction or boundary between semiconductor and organic materials due to the dipole-dipole interaction. Hybrid exciton formation in different systems has been studied in different geometrical configurations [1, 2, 4, 6, 7, 9, 10, 16] and has been shown to possess many desirable properties such as large exciton Bohr radius, large oscillator strength and high optical nonlinearities.

Large exciton radius especially favors polariton-polariton interaction and increases the operational temperature. The coupling of the two states is enhanced if the respective energy levels are in or near resonance. The hybridization of exciton state suggests using the organic component to dramatically enhance the operational temperature and the optical nonlinearities of inorganic structures. The observation of cavity mediated hybridization of GaAs and J-aggregate exciton in the strong coupling regime under electrical injection of carriers and the polariton lasing up to 200 K under non-resonant optical pumping [12] open the doors for successful realization of an inorganic-organic hybrid polariton laser with stable high polariton operational temperature and highly efficient electrical injection in the very near future. Recent work [11] shows that, by electrically injecting electron-hole pairs into the inorganic quantum-well system, a transfer of energy between cavities is possible, populating organic-exciton polaritons and exploring a new

way to facilitate energy transfer between semiconductor materials.

In this work we theoretically study the generalized model of hybrid excitons and hybrid polaritons in different geometric configurations. In addition to the effects certain parameters have on a system, numerical models of the dispersion relation of each system's hybrid polariton, all within an *ab initio* framework, are analyzed in order to discuss specific environments that promote the most favorable attributes of the system. From this theoretical information and the use of empirical data, we are then able to suggest components of heterostructures that foster ideal systems tailored to need and application.

1.1 Excitations as Quasiparticles

There are many ways to articulate the formation of the quasiparticles resulting from atomic or molecular excitations i.e., the phenomenon termed exciton. The most basic of those describes the *desire* that a particular electron has to return from a higher energy state to a ground state. More specifically, an electron in its maximum valence band state is excited to a minimum conduction band state, leaving a vacancy in the valence band continuum, called a *hole*. This vacancy induces a positive charge which attracts the newly created conduction band electron. The coulomb force is the *desire* spoke of earlier, and this process continues as long as the material is radiated with photons exceeding the band gap energy. Interestingly, this phenomenon i.e., the simultaneous creation of both a conduction band electron and a valence band hole, propagates through the periodic potential lattice and can be described using Bloch-function theory. Through this lens, the excitation is viewed as a single quasiparticle, having its own material-specific dispersion.

1.2 Geometry and its Influence

As we are well aware, geometry plays a very important role when considering quantum mechanical systems. In the case of excitons, this is no exception. We consider bulk materials to have a band gap continuum whereas quantum-confined structures, such as the quantum dots we regard in this work, exhibit discrete electronic transitions. Due to the latter case, quantum dots are often referred to as *artificial atoms*. Quantum dots are not the only quantum confinement nanostructure we can study. Actually, as theorists, our imagination is the limit.

This work examines a specific case, **Fig. 1a**, in which a quantum dot of inorganic semiconductor material, what we will refer to as the *core*, is coated by an organic material, what we will refer to as the *shell*. As we stated, there are other geometries one could take into account. Quantum wires, for example, are long cords of electronic material that have a diameter on the nanoscale. The most important aspect of geometry, though, is its dimensionality. We say that the quasiparticle has 3D mobility in bulk materials, 2D mobility in quantum wells (e.g. thin films), 1D mobility in quantum wires and rods, and 0D mobility in quantum dots, for example. It is this confinement in all directions of the quantum dot systems and the formation of discrete exciton states that we are particularly interested in because of the *tunability* of the band gap.

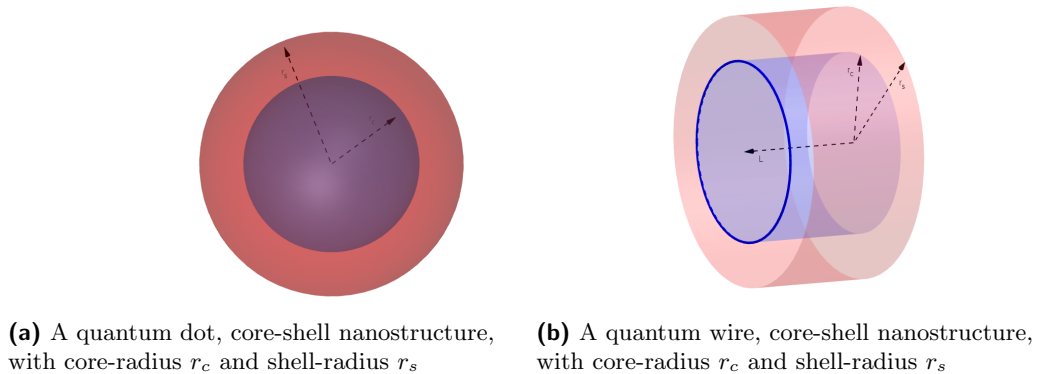


Figure 1. Two examples of different heterostructure geometries.

For the quantum dot system, we will assume the structure as spherically symmetric. In the spherical, three-dimensional quantum well, we recall that the quantized energy states for the *particle in a box* is inversely proportional to the squared radius of the spherical well, $\sim 1/a^2$. Thus, the energy levels have a strong dependence on the confinement size, and we will see later that we consider a *weak confinement regime* that insures adequate dependence on both the core material's exciton Bohr radius and the core size.

CHAPTER 2

EXCITON HYBRIDIZATION

2.1 Coupled Two-Oscillator Dispersion

Let us consider a structure consisting of a semiconductor component and an organic component. The theory could be applied for different semiconductor-organic heterostructures. One of the examples is a semiconductor quantum dot coated by an organic shell. The total Hamiltonian of the system of interacting Wannier excitons and Frenkel excitons, using the rotating wave approximation (RWA), will be taken as follows:

$$H_\alpha = H_F + H_W + H_{F-W} = \sum_{\mathbf{k}} \left[E_{\mathbf{k}}^F \hat{a}_{\mathbf{k}}^\dagger \hat{a}_{\mathbf{k}} + E_{\mathbf{k}}^W \hat{b}_{\mathbf{k}}^\dagger \hat{b}_{\mathbf{k}} + \Gamma_{\mathbf{k}} (\hat{a}_{\mathbf{k}}^\dagger \hat{b}_{\mathbf{k}} + \hat{b}_{\mathbf{k}}^\dagger \hat{a}_{\mathbf{k}}) \right], \quad (2.1)$$

where H_F is the Frenkel exciton Hamiltonian, H_W is the Wannier Mott exciton Hamiltonian and H_{F-W} is the interaction Hamiltonian between the Wannier Mott excitons in the organic component and the Frenkel excitons in the organic component with coupling constant $\Gamma_{\mathbf{k}}$. $E_{\mathbf{k}}^W$ and $E_{\mathbf{k}}^F$ are the excitation energies of Wannier excitons in the organic material and the Frenkel exciton in the organic medium, respectively. $\hat{a}_{\mathbf{k}}^\dagger$ ($\hat{a}_{\mathbf{k}}$) are creation (annihilation) operators of Frenkel excitons, $\hat{b}_{\mathbf{k}}^\dagger$ ($\hat{b}_{\mathbf{k}}$) are creation (annihilation) operators of Wannier excitons.

Applying the unitary transformation we can write the system as a pure hybrid exciton system as follows

$$H_\alpha = \sum_{\mathbf{k}} E_{\mathbf{k}}^\alpha \hat{\alpha}_{\mathbf{k}}^\dagger \hat{\alpha}_{\mathbf{k}}. \quad (2.2)$$

where $\hat{\alpha}_{\mathbf{k}}^\dagger$ ($\hat{\alpha}_{\mathbf{k}}$) are creation (annihilation) operators of the Wannier-Frenkel exciton, and $E_{\mathbf{k}}^\alpha$ are the energies of the hybrid exciton. When the energies of Wannier and Frenkel excitons are comparable (i.e., when the energy separation between the Wannier-Mott and the Frenkel excitons is much less than the distance to other exciton bands) and the mixing state is assumed only between the two nearest bands, the basis of the hybridization is chosen such that when the Wannier-Mott exciton is in its excited state the Frenkel exciton is in its ground state and vice

versa. We have the following:

$$|\Psi(\mathbf{k})\rangle = u_l(\mathbf{k})f^F(0)|\Psi_l^W(\mathbf{k})\rangle + v_l(\mathbf{k})f^W(0)|\Psi_l^F(\mathbf{k})\rangle, \quad (2.3)$$

with the branch-energy $E(\mathbf{k})$ of the hybrid state given as

$$E_j^\alpha(\mathbf{k}) = \frac{1}{2} \left(E_{\mathbf{k}}^F + E_{\mathbf{k}}^W \pm \sqrt{(E_{\mathbf{k}}^F - E_{\mathbf{k}}^W)^2 + 4\Gamma_{\mathbf{k}}^2} \right). \quad (2.4)$$

The energy of the hybrid exciton as a function of \mathbf{k} , is shown in **Fig. 2a**, and the mixing coefficients for the upper hybrid exciton branch are shown in **Fig. 2b**, where the Frenkel exciton energy is considered independent of the wave vector \mathbf{k} .

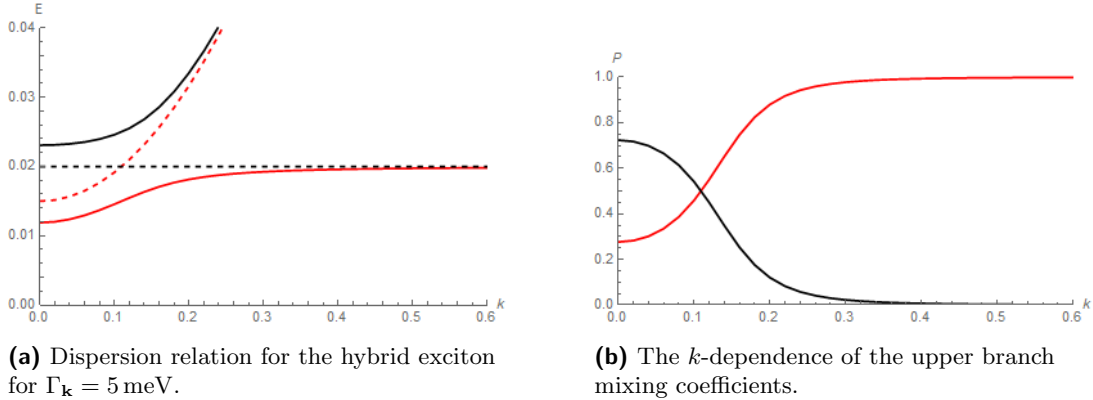


Figure 2. Example of a hybrid exciton dispersion and branch mixing. The red and black curves reflect the red and black dotted curves of the pure states on the dispersion graph, respectively.

A common term is used to identify the difference in constituent energies, the *detuning* of the system. In this case, $\Delta = E_{\mathbf{k}}^F - E_{\mathbf{k}}^W$ is the detuning parameter for our two hybridized exciton species, and its value clearly affects several aspects of the system. Other than being present in the radicand of the eigenenergies, it shows up, not surprisingly, in the mixing coefficients. These coefficients also influence the lifetime of the hybrid exciton. Finally, we remind ourselves that the curvature of the dispersion is inversely proportional to the effective mass of the quasiparticle. The detuning parameter plays a prominent role in the branch formation, and therefore, it can be used to alter the effective mass of the hybrid exciton.

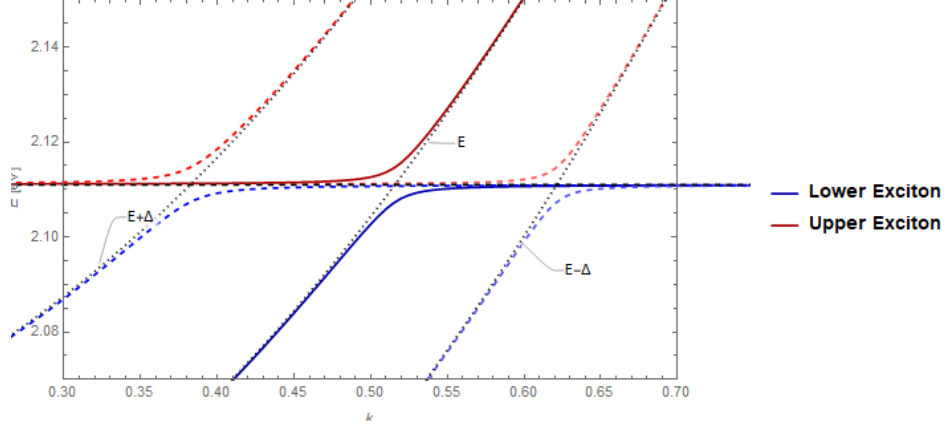


Figure 3. An example of the hybrid exciton dispersion curve shifting in response to a change in the detuning of the system by 50meV.

2.2 Wannier-Frenkel Exciton Hybridization

The coupling constant (i.e., the hybridization parameter), $\Gamma_{\mathbf{k}}$, stands for the dipole-dipole interaction between excitons, taken as the product of the operator of the electric field $E(r)$ created at point r in the organic medium by the excitons in quantum dots and the transition polarization operator $P(r)$ of the Frenkel exciton at molecular site r of the organic shell-medium,

$$\Gamma_{\mathbf{k}} = \langle F_u, \mathbf{k} | U | W_v, \mathbf{k} \rangle, \quad (2.5)$$

where, for the case of a semiconductor quantum dot with an organic shell heterostructure as diagrammed in **Fig. 4**, U is the interaction of the dipoles of the Frenkel exciton in the shell and the Wannier exciton in the semiconductor core. For the coated quantum dot heterostructure, let the dielectric constants for the dot core and shell be ϵ_c and ϵ_s respectively. For this we have,

$$U = \frac{3\epsilon_c}{2\epsilon_s + \epsilon_c} \frac{(\vec{\mu}_F \cdot \vec{\mu}_W) - 3(\vec{\mu}_W \cdot \hat{r})(\vec{\mu}_F \cdot \hat{r})}{4\pi\epsilon_0 r^3}. \quad (2.6)$$

Then the coupling constant **(2.6)** will be calculated for each of the excited states $u \neq v \in \{0, 1\}$, which denotes respective ground states and first excited states.

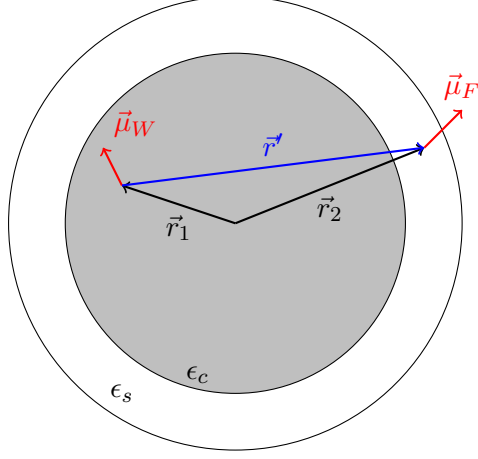


Figure 4. The dipole moments of excitons in a quantum dot with organic shell.

In [4], Engelmann and coauthors obtained the coupling constant as

$$\Gamma = -\frac{32\mu_W\mu_F}{15\epsilon} \sqrt{\frac{\pi R_D^3}{2a_B^3 V_{\text{cell}} d_0^3} \delta_2}, \quad (2.7)$$

where ϵ is an approximated dielectric function, d_0 is the thickness of the organic shell, R_D is the radius of the quantum dot core, V_{cell} is the cell volume of the organic crystal lattice, and δ_2 is a polar-angle dependent, non-uniformity factor Engelmann et al. includes for the shell thickness.

The problem with this solution in terms of application is that one must carefully choose effective dielectric constants for the model prior to extrapolating data for suitable semiconductor materials. Rather, one must either choose a *good* effective dielectric constant for the system, then figure out the heterostructure makeup like Bohr radius, or vice-versa. Attacking the problem in this manner would be incredibly inefficient and could have wrong assumptions.

We define ϵ using an internal homogenization effective medium theory (IH EMT). The particular function used is

$$\frac{\epsilon - 1}{\epsilon + 2} = \frac{(\epsilon_s - 1)(\epsilon_c + 2\epsilon_s) + f(\epsilon_c - \epsilon_s)(1 + 2\epsilon_s)}{(\epsilon_s + 2)(\epsilon_c + 2\epsilon_s) + 2f(\epsilon_s - 1)(\epsilon_c - \epsilon_s)}, \quad (2.8)$$

where $f = \left(\frac{R_c}{R_s}\right)^3$, the fraction of the overall sphere volume that the dot core occupies i.e., the *filling factor*. In this process, the polarizability of the equivalent sphere is equated to that of a core-shell in the electrostatic approximation. Note that **(2.8)** is independent of the particle size

and is only valid in the regime for which the particle size is much smaller than the incident wavelength [8]. We solve (2.8) for the effective dielectric constant and further express the solution in terms of a new quantity η , the ratio of the inorganic core dielectric constant to the organic shell-material dielectric constant

$$\epsilon = \epsilon_s \frac{\eta(1 + 2f) + 2(1 - f)}{\eta(1 - f) + (2 + f)}. \quad (2.9)$$

As one can see, we now have an equation that allows us to analyze the hybridization parameter in terms of the core material, if we choose. This is more desirable for experimentalists because inorganic material have been studied in far greater detail and possess more predictable electronic characteristics. Ideally, we would like to reduce the number of parameters in the mixing coefficient to such an extent that heterostructures could be easily determined using very few semiconductor properties and have their optoelectrical properties closely predicted.

This hybridization parameter, expressed in terms of the filling factor, allows us to examine the system in terms of a ratio relating the core radius and shell thickness,

$$\Gamma = -\frac{32\eta[\eta(1 - f) + (2 + f)]\mu_W\mu_F}{15\epsilon_c[\eta(1 + 2f) + 2(1 - f)]} \delta_2 \sqrt{\frac{\pi f}{2a_B^3 a_{L'}^3 (1 - \sqrt[3]{f})^3}}. \quad (2.10)$$

We have also taken the liberty of writing the unit cell volume of the organic lattice as an *isometrized* lattice constant, simply defined as $a_{L'} \equiv \sqrt[3]{V_{\text{cell}}}$. For example, reported lattice parameters for perylene suggest a unit cell volume of around 1230 Å³, which translates to an *isometrized* lattice constant of around 10.7 Å [5]. The reason for this is to further help us estimate other properties of the heterostructures without compromising earlier work.

The existence of the Wannier-Mott exciton in the dot will restrict our core sizes to those that foster weak-confinement conditions in addition to nonlinear susceptibilities. As detailed in [4], desired optoelectrical characteristics of the core-shell heterostructure depend significantly on a large, *but not too large*, and small, *but not too small*, core radius. We must determine a regime in which the semiconductor excitons interact, allowing for nonlinear optical properties, and the weak-confinement limit is obeyed [4]. In a least restrictive domain, we take the lower bound and

upper bound for the core radius as $a_B \leq R_c \leq R_{\max}$. As discussed by Steiner, this upper bound should be no larger than 10 nm for a certain room temperature heterostructure [15].

For ϵ_c , using calculated Bohr radii and generally accepted experimental dielectric constants of various common semiconductor materials, we obtained a statistical fit relating exciton Bohr radii and dielectric constants

$$\epsilon_c \approx 2.28311 \ln \left[\frac{a_B \times 10^{10}}{0.628} \right]. \quad (2.11)$$

The fit, (2.11), calculated from the data in **Fig. 5**, is a characteristic of this model that should be adjusted as more experimental and theoretical data become available. More accurate curve-fitting will enhance the model and allow for more predictable heterostructures; however, it is worth noting that any appreciable error would come out of a material dielectric ratio larger than the one considered here due to the current list of available and common materials for heterostructure fabrication falling within this small domain. With this expression of ϵ_c , the

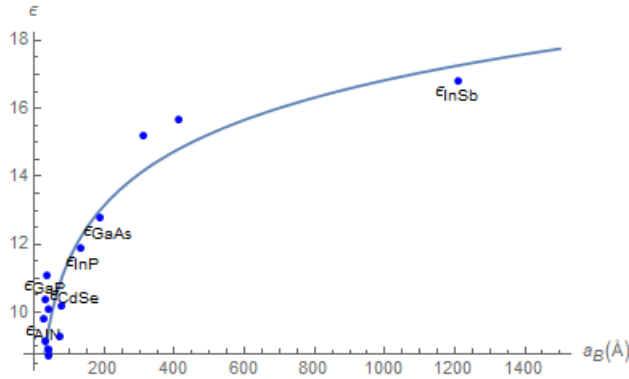


Figure 5. Calculated Bohr radii and dielectric constants for various common, inorganic semiconductor materials with logarithmic curve-fitting.

hybridization parameter can be expressed in terms of the materials' dipole moments, in addition to the ratio of their dielectric constants, the filling factor, the core Bohr radius and the organic material unit cell volume.

2.3 Numerical Analysis of Engelmann's, et al. Hybridization Parameter

From the results obtained in 2.1, a density plot of the hybridization coefficient is presented in **Fig. 6**, where both dipole moments are valued at 1 D, a *non-uniformity factor* [4] of

$\frac{1}{10}$, and an isometric organic lattice constant of 5 \AA . **Fig. 6a** allows us to ascertain heterostructures that exhibit specific exciton hybridization between the organic shell and inorganic core. As an example, one might achieve a hybridization parameter magnitude $\approx 15 \text{ meV}$ for a core-shell nanoparticle (CSNP) with a Wannier-Mott exciton Bohr radius of around 50 \AA , an inorganic dielectric constant between 2 to 3 times the organic shell material dielectric constant, and a CSNP filling factor greater than about 0.6.

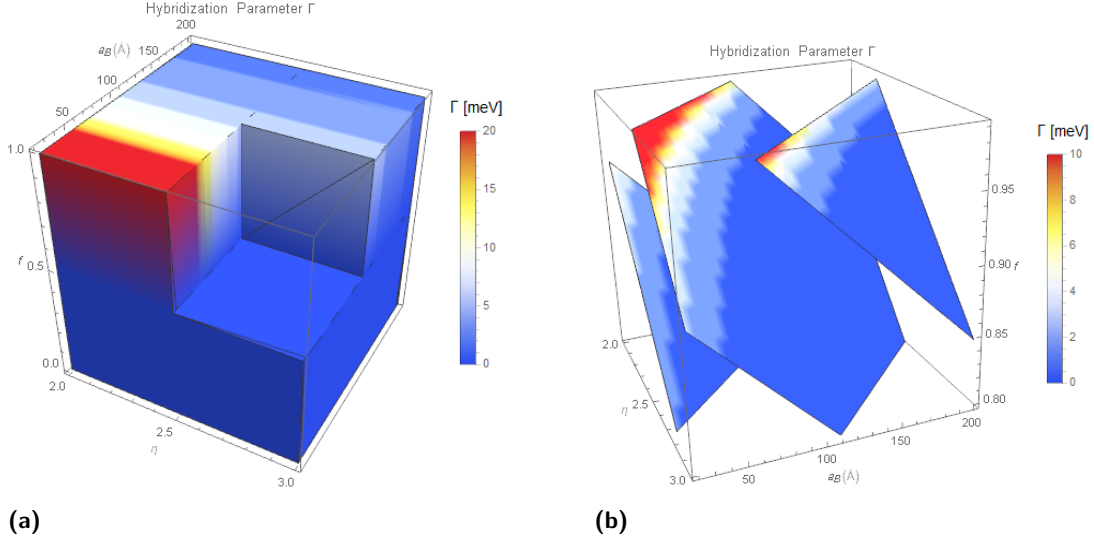


Figure 6. Density plots for the hybridization parameter dependent on the semiconductor exciton Bohr radius, the core-shell filling factor, and the ratio of inorganic to organic dielectric constants.

From **Fig. 6a**, it is still difficult to tell how one achieves a specific interaction value; however, the following plot, **Fig. 6b**, demonstrates the subtle effect the filling factor has on the system. It is interesting, and strange, to note that the dielectric ratio η plays a very small role in the hybridization parameter. **Fig. 7** shows just how negligible the parameter is if we consider only values between 2 to 3. Given a much larger domain, one which at present may be overly estimating our choices for organic materials, we can see that the dielectric ratio becomes significant just outside of the bound we consider, i.e. $\eta \gtrsim 3$, and only to a factor of around $\frac{1}{10}$.

It is somewhat of a subtlety, and worth mentioning, how influential the non-uniformity factor is in the hybridization between the two exciton species. A degree of *roughness* at the interface of the core and shell could potentially be exploited to repress any shortcoming with other parameters of the system. We take special notice of this because altering any, say, *lengths*

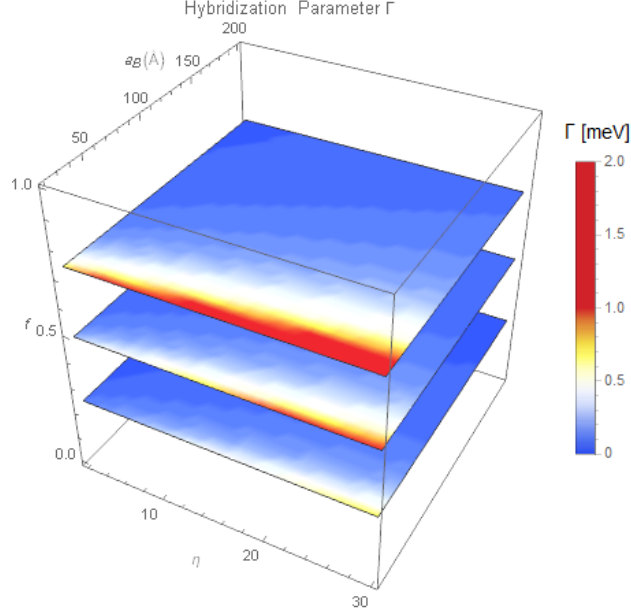


Figure 7. A sliced density plot that illustrates the relatively negligible influence that the dielectric ratio has on the hybridization parameter.

as a parameter is more tedious to track. Stated better perhaps, once we choose our heterostructure materials, we want to stick with them. Thus, we look to tailor other variables to enhance a desired attribute of the system. This would include the interface *roughness* and the average thickness of the shell. Though it is clear from (2.10) to what degree this non-uniformity affects the interaction, **Fig. 8** helps us visualize how significant of a parameter it is.

2.4 Organic-Inorganic Exciton Optical Nonlinearity

The optical nonlinear susceptibility, χ , for the hybrid exciton at resonance, again detailed in [4], as a ratio with respect to the Frenkel species of exciton has orders of magnitude plotted in **Fig. 9** against the filling factor for the CSNP heterostructure. The three different plots refer to three various ratios of the average shell thickness, d_0 , to the *isometrized* organic lattice constant, $a_{L'}$,

$$\frac{P_{HY-}^{(3)}}{P_F^{(3)}} \sim 4\pi \left(\frac{d_0}{a_{L'}} \right)^3 \left(\frac{\sqrt[3]{f}}{1 - \sqrt[3]{f}} \right)^2. \quad (2.12)$$

It is obvious that the hybridization is a critical ingredient in enhancing the third-order nonlinearity.

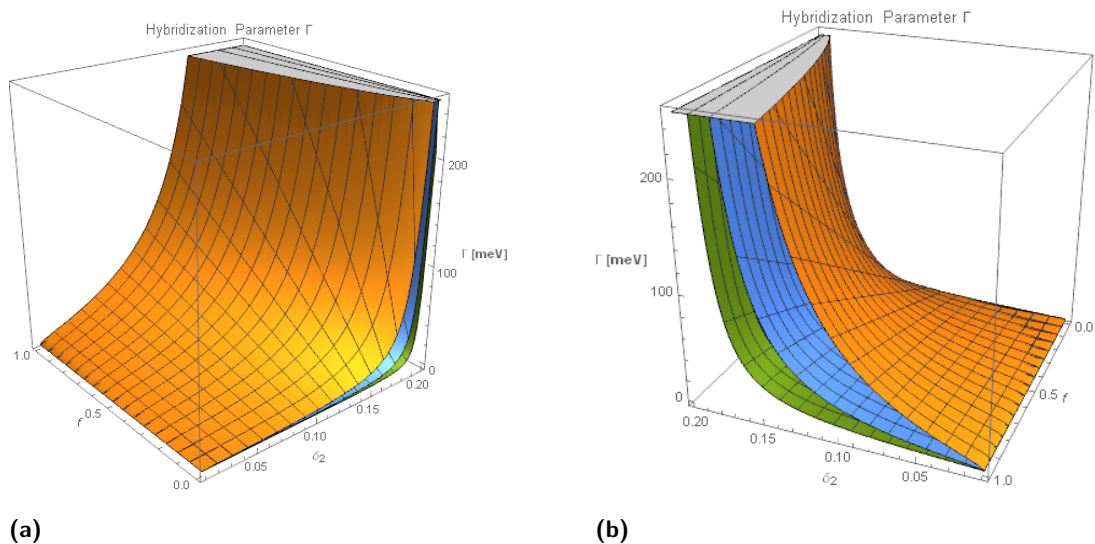


Figure 8. Surface plots for three different core-exciton Bohr radii to illustrate the significance of the core-shell interface *roughness*.

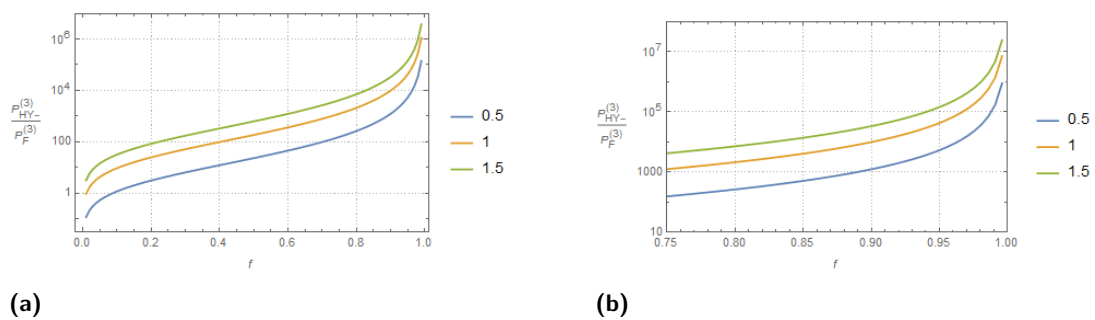


Figure 9. A log-plot for the rough orders of magnitude of third-order nonlinearity ratios dependent on the CSNP filling factor. Each curve is a different average shell thickness to organic lattice constant ratio. **b)** is the desired filling factor region.

CHAPTER 3

HYBRID EXCITON-POLARITON

3.1 Coupled Three-Oscillator Dispersion

We study the formation of organic-inorganic hybrid excitonic polariton by excitation of an organic-inorganic heterostructure in a microcavity by an optical wave. As noted above, the organic-inorganic hybrid exciton has a large exciton radius from the inorganic component and a very large oscillator strength from the organic component, all in addition to an increased optical nonlinearity by 2 orders. At resonance, the hybridization will encourage the formation of the polariton at high temperatures.

We consider a semiconductor-organic system in the RWA consisting of the Wannier-Mott exciton, the Frenkel exciton, and the photon with interaction between them

$$\begin{aligned}
 H_\pi &= H_F + H_W + H_{F-W} + H_\gamma + H_{F-\gamma} + H_{W-\gamma} \\
 &= \sum_{\mathbf{k}} E_{\mathbf{k}}^F \hat{a}_{\mathbf{k}}^\dagger \hat{a}_{\mathbf{k}} + E_{\mathbf{k}}^W \hat{b}_{\mathbf{k}}^\dagger \hat{b}_{\mathbf{k}} + \Gamma_{\mathbf{k}} (\hat{a}_{\mathbf{k}}^\dagger \hat{b}_{\mathbf{k}} + \hat{b}_{\mathbf{k}}^\dagger \hat{a}_{\mathbf{k}}) + E_{\mathbf{k}}^\gamma \hat{c}_{\mathbf{k}}^\dagger \hat{c}_{\mathbf{k}} + \\
 &\quad + \zeta_{\mathbf{k}} (\hat{a}_{\mathbf{k}}^\dagger \hat{c}_{\mathbf{k}} + \hat{c}_{\mathbf{k}}^\dagger \hat{a}_{\mathbf{k}}) + \xi_{\mathbf{k}} (\hat{b}_{\mathbf{k}}^\dagger \hat{c}_{\mathbf{k}} + \hat{c}_{\mathbf{k}}^\dagger \hat{b}_{\mathbf{k}}),
 \end{aligned} \tag{3.1}$$

where H_γ is the pure photon Hamiltonian, $H_{F-\gamma}$ and $H_{W-\gamma}$ are the interaction Hamiltonians describing the coupling between the Frenkel exciton and photon with coupling constant $\zeta_{\mathbf{k}}$ and the Wannier-Mott exciton and photon with coupling constant $\xi_{\mathbf{k}}$ respectively.

We will obtain the pure hybrid polariton-system

$$H_\pi = \sum_{\mathbf{k}} E_{\mathbf{k}}^\pi \hat{\pi}_{\mathbf{k}}^\dagger \hat{\pi}_{\mathbf{k}}. \tag{3.2}$$

In matrix notation, the Hamiltonian can be written as,

$$\sum_{\mathbf{k}} E_{\mathbf{k}}^\pi \hat{\pi}_{\mathbf{k}}^\dagger \hat{\pi}_{\mathbf{k}} = \sum_{\mathbf{k}} \begin{pmatrix} \hat{a}_{\mathbf{k}}^\dagger & \hat{b}_{\mathbf{k}}^\dagger & \hat{c}_{\mathbf{k}}^\dagger \end{pmatrix} B \begin{pmatrix} \hat{a}_{\mathbf{k}} \\ \hat{b}_{\mathbf{k}} \\ \hat{c}_{\mathbf{k}} \end{pmatrix} \tag{3.3}$$

where B , the interaction matrix for the system, is

$$B = \begin{pmatrix} E_{\mathbf{k}}^{\gamma} & \zeta_{\mathbf{k}} & \xi_{\mathbf{k}} \\ \zeta_{\mathbf{k}} & E_{\mathbf{k}}^F & \Gamma_{\mathbf{k}} \\ \xi_{\mathbf{k}} & \Gamma_{\mathbf{k}} & E_{\mathbf{k}}^W \end{pmatrix} \quad (3.4)$$

Applying the unitary transformation U ,

$$\begin{pmatrix} \hat{a}_{\mathbf{k}} \\ \hat{b}_{\mathbf{k}} \\ \hat{c}_{\mathbf{k}} \end{pmatrix} = U \begin{pmatrix} \hat{\pi}_{\mathbf{k}1} \\ \hat{\pi}_{\mathbf{k}2} \\ \hat{\pi}_{\mathbf{k}3} \end{pmatrix} \quad (3.5)$$

we obtained the system of equations for the mixing coefficients

$$\begin{pmatrix} E_{\mathbf{k}}^{\gamma} - E_{\mathbf{k}1}^{\pi} & \zeta_{\mathbf{k}} & \xi_{\mathbf{k}} \\ \zeta_{\mathbf{k}} & E_{\mathbf{k}}^F - E_{\mathbf{k}2}^{\pi} & \Gamma_{\mathbf{k}} \\ \xi_{\mathbf{k}} & \Gamma_{\mathbf{k}} & E_{\mathbf{k}}^W - E_{\mathbf{k}3}^{\pi} \end{pmatrix} \begin{pmatrix} u_{1j} \\ u_{2j} \\ u_{3j} \end{pmatrix} = 0. \quad (3.6)$$

This gives the characteristic equation

$$\begin{aligned} & (E_{\mathbf{k}j}^{\pi} - E_{\mathbf{k}}^{\gamma})(E_{\mathbf{k}j}^{\pi} - E_{\mathbf{k}}^F)(E_{\mathbf{k}j}^{\pi} - E_{\mathbf{k}}^W) + \dots \\ & \dots - [\Gamma_{\mathbf{k}}^2(E_{\mathbf{k}j}^{\pi} - E_{\mathbf{k}}^{\gamma}) + \zeta_{\mathbf{k}}^2(E_{\mathbf{k}j}^{\pi} - E_{\mathbf{k}}^W) + \xi_{\mathbf{k}}^2(E_{\mathbf{k}j}^{\pi} - E_{\mathbf{k}}^F) + 2\Gamma_{\mathbf{k}}\zeta_{\mathbf{k}}\xi_{\mathbf{k}}] = 0. \end{aligned} \quad (3.7)$$

Reduction to a depressed cubic and then exploiting the fact that we will have three real roots, we use François Viète's trigonometric formulae [14] to produce the following eigenenergies for the hybrid polariton:

$$E_{\mathbf{k}j}^{\pi} = 2\sqrt{-\frac{p}{3}} \cos \left(\frac{1}{3} \arccos \left(\frac{3q}{2p} \sqrt{\frac{-3}{p}} \right) - \frac{2\pi(j-1)}{3} \right) + \frac{E_{\mathbf{k}}^{\gamma} + E_{\mathbf{k}}^F + E_{\mathbf{k}}^W}{3}, \quad (3.8)$$

where $j = \{1, 2, 3\}$ we define the following:

$$p = \frac{3a_1 - a_2^2}{3},$$

and

$$q = \frac{2a_2^3 - 9a_1a_2 + 27a_0}{27}$$

given the secular equation coefficients

$$a_2 = -(E_{\mathbf{k}}^\gamma + E_{\mathbf{k}}^F + E_{\mathbf{k}}^W),$$

$$a_1 = E_{\mathbf{k}}^F E_{\mathbf{k}}^W + E_{\mathbf{k}}^\gamma E_{\mathbf{k}}^W + E_{\mathbf{k}}^\gamma E_{\mathbf{k}}^F - (\Gamma_{\mathbf{k}}^2 + \zeta_{\mathbf{k}}^2 + \xi_{\mathbf{k}}^2),$$

and

$$a_0 = \Gamma_{\mathbf{k}}^2 E_{\mathbf{k}}^\gamma + \zeta_{\mathbf{k}}^2 E_{\mathbf{k}}^W + \xi_{\mathbf{k}}^2 E_{\mathbf{k}}^F - (E_{\mathbf{k}}^\gamma E_{\mathbf{k}}^F E_{\mathbf{k}}^W + 2\Gamma_{\mathbf{k}} \zeta_{\mathbf{k}} \xi_{\mathbf{k}}).$$

We include the details of Viète's formulae for the purpose of gathering potential insight into the structure of the polariton branches.

For the energy of the microcavity photon and refractive index n , we use a well known result [13] and note that the wavevector component along the length of the cavity is $k_z = \frac{\pi}{L}$ while taking the in-plane, parallel component as $k_{||} = E_\theta^\gamma \frac{\sin \theta}{\hbar c}$. Therefore, the cavity mode energy with angle of incidence dependence is $E_\theta^\gamma = E_0^\gamma \left[1 - \frac{\sin^2 \theta}{n^2} \right]^{-1/2}$ and the Frenkel exciton and Wannier-Mott exciton energies are taken as $E_{\mathbf{k}}^F = E_0^W + \Delta$ and $E_{\mathbf{k}}^W = E_0^W$, respectively. The eigenenergies of the hybrid polariton can be plotted as a function of the angle of incidence θ , as shown in **Fig. 10**, where $\Gamma_{\mathbf{k}}$ in this case is considered vanishingly small.

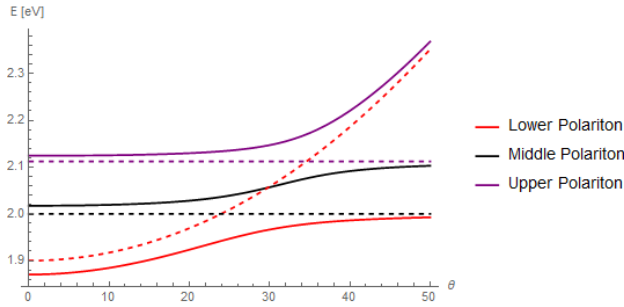


Figure 10. Relationship between the angle of incidence θ and the polariton energy.

Additionally, the mixing coefficients for the lower, middle, and upper hybrid polariton branches are plotted in **Fig. 11a**, **Fig. 11b**, and **Fig. 11c** respectively. Note the change of the

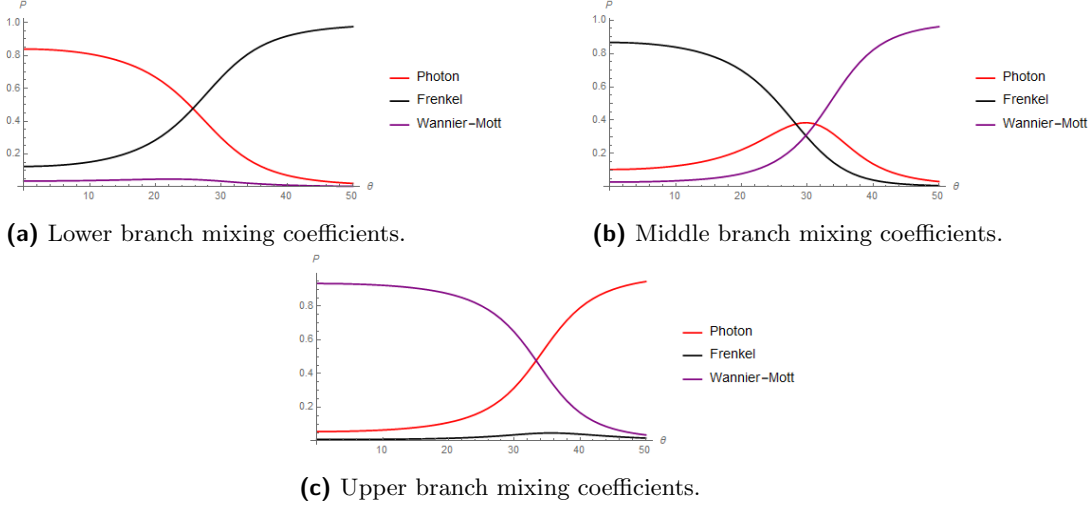


Figure 11. Relationship between the angle of incidence θ and the branch mixing coefficients.

mixing coefficients, or the weights of different excitonic species in the different branches of the mixed polariton state. This suggests choosing the branch suitable for the application, depending on the preferred properties of a specific excitonic species.

3.2 Numerical Analysis of the Hybrid Polariton

For two cases of the hybrid polariton, the eigenenergies and middle branch mixing coefficients are plotted alongside one another without the explicit consideration of a microcavity (here we assume the photon coupling but neglect the apparatus that ensures it) with exciton energies as those approximated using the Brus equation, i.e. using the effective mass approximation, and the photon energy as $E_{\mathbf{k}} = c\hbar k$. As shown in **Fig. 12**, the initial Frenkel exciton energy is 2.11 eV, initial Wannier-Mott exciton energy is 2 eV, and the heterostructures are such that they yield hybridization values of 1 meV and 30 meV. Both exciton-photon interaction potentials are valued as 50 meV. From the results of the middle branch mixing, we see that, by increasing the hybridization between the constituent excitons, one exciton density is suppressed at near resonance for the system while stronger photon-exciton coupling occurs with the other. In addition, the equal mixing of photon and both excitons are shifted somewhat.

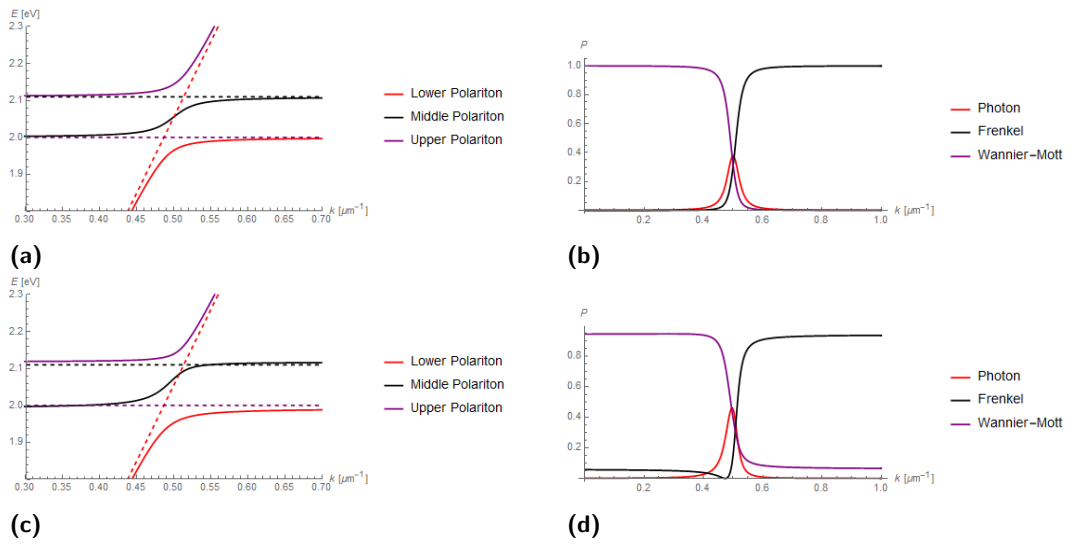


Figure 12. The dispersion and middle branch mixing curves for the hybrid polariton in the case of a CdSe core. **a)** and **b)** illustrate the case when the hybridization parameter is 1 meV, while **c)** and **d)** depict the case when the hybridization parameter is 30 meV.

CHAPTER 4

STARK EFFECT ON HYBRID EXCITONS

The Wannier-Mott exciton, with its incredibly large Bohr radius, is more susceptible than the Frenkel exciton to perturbation. This fact is a primary influence for studying a hybridization that includes the Wannier exciton. Specifically, we are looking at the lifting of degenerate states due to the presence of an external electric field, and consider only the effects the applied electric field has on this component of the hybrid exciton. We write the Wannier-Mott exciton in the core structure as a product state, such that

$$|\Psi_l^W(\mathbf{r})\rangle = |\psi_\alpha(\mathbf{r}_e)\rangle|\psi_\beta(\mathbf{r}_h)\rangle. \quad (4.1)$$

4.1 The Electron and Hole in a Quantum Dot of known Radius

The electron wavefunction in a spherically symmetric potential well i.e., our quantum dot, is already well known. In this work, we consider only the first excited state of the Wannier-Mott exciton, with electron function as

$$\psi_\alpha(r_e) = \xi(r)|S\alpha\rangle = \sqrt{\frac{2}{a}} \frac{\sin\left(\frac{\pi r_e}{a}\right)}{r_e} Y_{00}|S\alpha\rangle, \quad (4.2)$$

where a is the quantum dot radius, r_e is the position of the electron within the sphere, $Y_{l,m}$ are the usual spherical harmonic functions, and $|S\alpha\rangle$ are the conduction band states. [3]

The hole, however, has a far more complicated set of wavefunctions due to the spin-orbit interaction in the valance band. Efros, et al. considers this and that l is no longer a *good* quantum number when dealing with perturbations such as the Stark Effect. We will need to examine it using the quantum number F , which we designate as the total angular momentum. Allowing $F = \{\frac{1}{2}, \frac{3}{2}, \dots\}$ and $M = \{-F, -F + 1, \dots, F\}$, the hole wavefunction for the quantum

dot takes the form

$$\begin{aligned} \psi_\beta(r_h) = \psi_{F,M}^\pm(r_h) = \sqrt{2F+1} \sum_{l=l_\pm} (-1)^{l+M-\frac{3}{2}} R_l^\pm(r_h) \sum_{\mu=-\frac{3}{2}}^{\frac{3}{2}} \langle l \frac{3}{2} F | m \mu - M \rangle Y_{l,m} u_{\frac{3}{2},\mu} + \dots \\ \dots + (-1)^{F \pm \frac{1}{2} - M} R_s^\pm(r_h) \sum_{\mu=-\frac{1}{2}}^{\frac{1}{2}} \langle F \pm \frac{1}{2} \frac{1}{2} F | m \mu - M \rangle Y_{F \pm \frac{1}{2}, m} u_{\frac{1}{2},\mu}, \end{aligned} \quad (4.3)$$

where $l_+ = \{F - \frac{3}{2}, F + \frac{1}{2}\}$, $l_- = \{F - \frac{1}{2}, F + \frac{3}{2}\}$, so called *odd* and *even* solutions respectively, and the coefficients in the last two sums are the familiar Wigner $3j$ -symbols. This work considers only the odd solutions i.e., $\psi_{F,M}^+(r_h)$. We take the radial functions for the quantum dot geometry as the usual

$$R_l = \sqrt{\frac{2}{a^3}} \frac{j_l(\lambda_{nl} \frac{r}{a})}{j_{l+1}(\lambda_{nl})}, \quad (4.4)$$

where j_l is the spherical Bessel function of order l , and λ_{nl} is the n -th zero of order l .

4.2 Stark Effect on the Hybrid Exciton

From 4.1 and taking the applied electric field as $\hat{E} = eE_0(r_e \cos \theta_e - r_h \cos \theta_h)$, we found that the only nonzero matrix elements are

$$\left\{ \left\langle \psi_\alpha \psi_{\frac{3}{2}, -\frac{1}{2}}^+ \left| \hat{E} \right| \psi_\alpha \psi_{\frac{1}{2}, -\frac{1}{2}}^+ \right\rangle, \left\langle \psi_\alpha \psi_{\frac{3}{2}, \frac{1}{2}}^+ \left| \hat{E} \right| \psi_\alpha \psi_{\frac{1}{2}, \frac{1}{2}}^+ \right\rangle \right\}, \quad (4.5)$$

this due to the orthonormality of the Bloch functions. Therefore, the nonzero matrix elements are expressed as

$$\begin{aligned} \left\langle \psi_\alpha \psi_{\frac{3}{2}, \pm \frac{1}{2}}^+ \left| \hat{E} \right| \psi_\alpha \psi_{\frac{1}{2}, \pm \frac{1}{2}}^+ \right\rangle = \\ = eE_0 \sqrt{\frac{4\pi}{3}} \left[\left\langle \psi_{\frac{3}{2}, \pm \frac{1}{2}}^+ \left| r_h Y_{10}^h \right| \psi_{\frac{1}{2}, \pm \frac{1}{2}}^+ \right\rangle \langle \psi_\alpha | \psi_\alpha \rangle - \left\langle \psi_{\frac{3}{2}, \pm \frac{1}{2}}^+ \left| \psi_{\frac{1}{2}, \pm \frac{1}{2}}^+ \right\rangle \langle \psi_\alpha | r_e Y_{10}^e | \psi_\alpha \rangle \right]. \end{aligned} \quad (4.6)$$

It is clear that the electron term will never satisfy the selection rule that $\Delta l = \pm 1$, so we concern ourselves only with the first hole term. Thus, with simplification, we have

$$\left\langle \psi_\alpha \psi_{\frac{3}{2}, \pm \frac{1}{2}}^+ \left| \hat{E} \right| \psi_\alpha \psi_{\frac{1}{2}, \pm \frac{1}{2}}^+ \right\rangle = \frac{eE}{3} \left[-\langle R_0^h | r_h | R_1^h \rangle + \frac{2}{5} \langle R_2^h | r_h | R_1^h \rangle \pm \frac{1}{5} \langle R_s^h | r_h | R_s^h \rangle \right] \langle \psi_\alpha | \psi_\alpha \rangle. \quad (4.7)$$

The twelve product states formed from the Γ_8 and Γ_7 symmetry in the valence band and the Γ_6 symmetry in the conduction band, comprise the ground state of the Wannier-Mott exciton confined in the core material. We need only construct the coefficient matrix for four of the twelve states that we found to have nontrivial inner products with the field hamiltonian. In matrix form, this is

$$W = \frac{eE_0}{a} \begin{pmatrix} 0 & 0 & A & 0 \\ 0 & 0 & 0 & B \\ A & 0 & 0 & 0 \\ 0 & B & 0 & 0 \end{pmatrix} \langle \psi_\alpha | \psi_\alpha \rangle, \quad (4.8)$$

for very complicated terms A and B containing various combinations of spherical Bessel functions, j_0, j_1, j_2, j_3 , and their roots, $\lambda_0, \lambda_1, \lambda_2$. The eigenvalues for this matrix are easily calculated by hand, so the perturbed energies can be written in the form $E_{+\frac{1}{2}} \pm \frac{eE_0}{a} A$ and $E_{-\frac{1}{2}} \pm \frac{eE_0}{a} B$, and are shown in **Fig. 13**. The radial matrix elements are individually calculated in **Appendix B**, and the first term, A , is approximated using truncated hypergeometric series.

To our knowledge, the Stark Effect for this sort of heterostructure has never been considered, especially so in the case of our model which accounts for the twelve hole states due to the very strong spin-orbit interaction in such a confinement. Splitting Wannier exciton energy will lead to the formation of new energy branches in the hybrid exciton, meaning that the tunability of an applied electric field creates another parameter which we can exploit for the purpose of further tailoring the CSNP to suit application. Additionally, altering the energy spectrum of the Wannier-Mott exciton in a predictable manner will consequently affect the hybridization between the two exciton species, shifting the resonance case by predictable wavevectors.

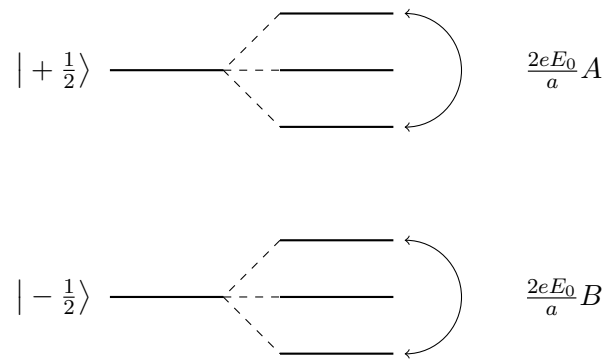


Figure 13. A schematic showing the predicted splitting of the two Wannier-Mott exciton states by respective factors due to an applied electric field.

CHAPTER 5

CONCLUSION

General models for both organic-inorganic excitons and polaritons are obtained, and an analytical discussion on the relationship between certain parameters and interactions is provided for the purpose of enhancing the hybridization between the materials. We emphasize tunability to suit application by leveraging system parameters that noticeably bias the system toward desired characteristics. The two different types of excitons, the Wannier-Mott and Frenkel excitons, both have characteristics that compliment each other when coupled in a heterostructure. This hybridized quasiparticle is a coherent superposition of quantum states and is tunable in the generalized, bulk system but known, *and verified in this work*, to be even more so in quantum confined geometries such as the core-shell nanoparticle we consider.

Through the rotating wave approximation, total-energy operators are constructed for the two hybrid quasiparticles of interest, the hybrid exciton and the hybrid exciton-polariton. The constituents interact with one another, and these potentials are carefully studied to determine conditions suitable for hybridization and tunability. Of these tuned characteristics, we looked at enhancing the interaction between the exciton species in the CSNP and found that the core-shell filling factor dominates as one of the most viable options for the significant adjustment of certain properties. Likewise, this filling factor is found to be a powerful influence in the third-order optical nonlinearity of this hybrid system. After thoroughly vetting the effects exciton hybridization has on certain desirable characteristics of the system, we continued on to the cavity-photon coupling with the CSNP hybrid exciton. Here, we found that one can suppress the density of one exciton type while simultaneously enhancing the photon-exciton coupling of the other.

Lastly, we considered an external electric field applied to the CSNP, noting that the large Bohr radius of the Wannier-Mott exciton makes it far more susceptible than the Frenkel exciton to such perturbations as the Stark Effect. The exciton's hole-wavefunction considers all three hole states in the inorganic semiconductor (states commonly referred to as heavy, light, and split-off) due to the spin-orbit interaction in the valence band, and this leads to quite complex expressions that required the use of hypergeometric series expansions to approximate energy-level splitting.

This computational exercise is believed to be a novel one, and we reach a theoretical conclusion otherwise unreported that, under these conditions, a predicted splitting of the Wannier-Mott exciton degenerate ground state occurs. From this splitting, new branches are formed for the hybrid exciton and another means for controlling its resonance case is obtained.

REFERENCES

- [1] V. M. Agranovich, Solid State Comm. **92** (1994), 295.
- [2] V. M. Agranovich, V. I. Yudson, and P. Reineker, *Electronic excitations in organic based nanostructures*, Elsevier Academic Press, 2003.
- [3] Al. L. Efros and M. Rosen, Phys. Rev. B **54** (1996), 4843.
- [4] A. Engelmann, V. I. Yudson, and P. Reineker, Phys. Rev. B **57** (1998), 1784.
- [5] I. A. Fedorov, Y. N. Zhuravlev, and V. P. Berveno, J. Chem. Phys. **138** (2013), 094509.
- [6] Y. Gao, N. Q. Huong, J. L. Birman, and M. J. Potasek, J. Appl. Phys. **96** (2004), 4839.
- [7] ———, Proc. SPIE Int. Soc. Opt. Eng. **5592** (2005), 272.
- [8] Yael Gutierrez, Dolores Ortiz, Rodrigo Alcaraz de la Osa, Juan M. Sanz, Jose M. Saiz, Francisco Gonzalez, and Fernando Moreno, *Evaluation of effective medium theories for spherical nano-shells*, e-print arXiv:1705.02248 [physics.optics], 2017.
- [9] N. Q. Huong and J. L. Birman, Phys. Rev. B **61** (1999), 13131.
- [10] ———, Phys. Rev. B **67** (2003), 075313.
- [11] R. Jayaprakash and et al., Light: Sci. Appl **8** (2019), 1.
- [12] S. G. Paschos and et al., Scientific Report **7** (2003), 1.
- [13] M. S. Skilnick, T. A. Fisher, and D. M. Whittaker, Semi. Sci. Tech. **13** (1998), 645.
- [14] G. W. Smith, *Cubic equation*, 2004 (accessed May 5, 2019), https://en.wikipedia.org/wiki/Cubic_equation.
- [15] T. D. Steiner, *Semiconductor nanostructures for optoelectronic applications*, Artech House, 2004.
- [16] V. I. Yudson, P. Reineker, and V. M. Agranovich, Phys. Rev. B **52** (1995), R5543.

APPENDIX A
APPROVAL LETTER



Office of Research Integrity

October 2, 2018

David Facemyer
Physics Department
Marshall University

Dear Mr. Facemyer:

This letter is in response to the submitted thesis abstract entitled "*Hybrid Excitations in Organic-Semiconductor Materials.*" After assessing the abstract, it has been deemed not to be human subject research and therefore exempt from oversight of the Marshall University Institutional Review Board (IRB). The Code of Federal Regulations (45CFR46) has set forth the criteria utilized in making this determination. Since the information in this study does not involve human subjects as defined in the above referenced instruction, it is not considered human subject research. If there are any changes to the abstract you provided then you would need to resubmit that information to the Office of Research Integrity for review and a determination.

I appreciate your willingness to submit the abstract for determination. Please feel free to contact the Office of Research Integrity if you have any questions regarding future protocols that may require IRB review.

Sincerely,

Bruce F. Day, ThD, CIP
Director

WE ARE... MARSHALL.

One John Marshall Drive • Huntington, West Virginia 25755 • Tel 304/696-4303
A State University of West Virginia • An Affirmative Action/Equal Opportunity Employer

APPENDIX B

SAMPLE CALCULATION FOR A-COEFFICIENT IN STARK EFFECT

The radial elements are:

$$\begin{aligned}\langle R_0^h | r_h | R_1^h \rangle &= \frac{2}{a^3 j_2(\lambda_{n1})} \int j_0\left(\lambda_{n0} \frac{r}{a}\right) j_1\left(\lambda_{n1} \frac{r}{a}\right) r dr \\ &= \frac{\pi}{a^2 j_2(\lambda_{n1}) \sqrt{\lambda_{n0} \lambda_{n1}}} \int J_{\frac{1}{2}}\left(\lambda_{n0} \frac{r}{a}\right) J_{\frac{3}{2}}\left(\lambda_{n1} \frac{r}{a}\right) r dr,\end{aligned}\tag{B.1}$$

$$\begin{aligned}\langle R_2^h | r_h | R_1^h \rangle &= \frac{2}{a^3 j_2(\lambda_{n1}) j_3(\lambda_{n2})} \int j_1\left(\lambda_{n1} \frac{r}{a}\right) j_2\left(\lambda_{n2} \frac{r}{a}\right) r dr \\ &= \frac{\pi}{a^2 j_2(\lambda_{n1}) j_3(\lambda_{n2}) \sqrt{\lambda_{n1} \lambda_{n2}}} \int J_{\frac{3}{2}}\left(\lambda_{n1} \frac{r}{a}\right) J_{\frac{5}{2}}\left(\lambda_{n2} \frac{r}{a}\right) r dr,\end{aligned}\tag{B.2}$$

and

$$\begin{aligned}\langle R_s^h | r_h | R_s^h \rangle &= \langle R_0^h | r_h | R_0^h \rangle = \frac{2}{a^3} \int j_0\left(\lambda_{n0} \frac{r}{a}\right)^2 r dr \\ &= \frac{\pi}{a^2 \lambda_{n0}} \int J_{\frac{1}{2}}\left(\lambda_{n0} \frac{r}{a}\right)^2 r dr.\end{aligned}\tag{B.3}$$

Bessel products from Gradshteyn and Ryzhik 8.442(1) are of the form

$$J_\nu(az) J_\mu(bz) = \frac{(az)^\nu (bz)^\mu}{2^{\nu+\mu} \Gamma(\mu+1)} \sum_{k=0}^{\infty} (-1)^k \left(\frac{az}{2}\right)^{2k} \frac{F(-k, -\nu-k; \mu-1; \frac{b^2}{a^2})}{k! \Gamma(\nu+k+1)},\tag{B.4}$$

where $F(-k, -\nu-k; \mu-1; \frac{b^2}{a^2})$ can conveniently be expressed as a hypergeometric series in Gradshteyn and Ryzhik 9.100, which are of the form

$$F(\alpha, \beta; \gamma; z) = 1 + \frac{\alpha\beta}{\gamma \cdot 1} z + \frac{\alpha(\alpha+1)\beta(\beta+1)}{\gamma(\gamma+1) \cdot 1 \cdot 2} z^2 + \frac{\alpha(\alpha+1)(\alpha+2)\beta(\beta+1)(\beta+2)}{\gamma(\gamma+1)(\gamma+2) \cdot 1 \cdot 2 \cdot 3} z^3 + \dots\tag{B.5}$$

We use this form due to the foresight that the terms will terminate quickly, as opposed to trying our hand at other integral forms. Evaluating the first four terms in the series that correspond to $\nu = \frac{1}{2}, \mu = \frac{3}{2}$ yield:

$$F\left(0, -\frac{1}{2}; \frac{1}{2}; \frac{b^2}{a^2}\right) = 1,\tag{B.6}$$

$$F\left(-1, -\frac{3}{2}; \frac{1}{2}; \frac{b^2}{a^2}\right) = 1 + 3 \frac{b^2}{a^2},\tag{B.7}$$

$$F\left(-2, -\frac{5}{2}; \frac{1}{2}; \frac{b^2}{a^2}\right) = 1 + 3 \frac{b^2}{a^2} + 5 \frac{b^4}{a^4},\tag{B.8}$$

$$F\left(-3, -\frac{7}{2}; \frac{1}{2}; \frac{b^2}{a^2}\right) = 1 + 3 \frac{b^2}{a^2} + 5 \frac{b^4}{a^4} + 7 \frac{b^6}{a^6}.\tag{B.9}$$

Then our expansion to $k = 3$ is

$$\begin{aligned}
J_{\frac{1}{2}}(\lambda_{n0}\frac{r}{a})J_{\frac{3}{2}}(\lambda_{n1}\frac{r}{a}) &= \frac{r^2}{4a^2\Gamma(\frac{5}{2})}\sqrt{\lambda_{n0}\lambda_{n1}^3}\sum_{k=0}^{\infty}(-1)^k\left(\frac{\lambda_{n0}r}{2a}\right)^{2k}\frac{F(-k, -\frac{1}{2}-k; \frac{1}{2}; \frac{\lambda_{n1}^2}{\lambda_{n0}^2})}{k!\Gamma(\frac{3}{2}+k)} \\
&= \frac{2r^2}{3\pi a^2}\sqrt{\lambda_{n0}\lambda_{n1}^3}\left[1 - \frac{2\left(\frac{\lambda_{n0}r}{2a}\right)^2}{3}\left(1 + 3\frac{\lambda_{n1}^2}{\lambda_{n0}^2}\right) + \frac{2\left(\frac{\lambda_{n0}r}{2a}\right)^4}{15}\left(1 + 3\frac{\lambda_{n1}^2}{\lambda_{n0}^2} + 5\frac{\lambda_{n1}^4}{\lambda_{n0}^4}\right) + \dots\right. \\
&\quad \dots - \frac{4\left(\frac{\lambda_{n0}r}{2a}\right)^6}{3 \cdot 7!!}\left(1 + 3\frac{\lambda_{n1}^2}{\lambda_{n0}^2} + 5\frac{\lambda_{n1}^4}{\lambda_{n0}^4} + 7\frac{\lambda_{n1}^6}{\lambda_{n0}^6}\right) + \dots \\
&\quad \left. + \frac{\sqrt{\pi}}{2}\sum_{k=4}^{\infty}(-1)^k\left(\frac{\lambda_{n0}r}{2a}\right)^{2k}\frac{F(-k, -\frac{1}{2}-k; \frac{1}{2}; \frac{\lambda_{n1}^2}{\lambda_{n0}^2})}{k!\Gamma(\frac{3}{2}+k)}\right].
\end{aligned} \tag{B.10}$$

We shall consider only the first four terms and omit $k \geq 4$. Thus our first matrix element is approximated as such,

$$\langle R_0^h | r_h | R_1^h \rangle \approx \frac{11.50}{a}. \tag{B.11}$$

This approach is used for the remaining two radial matrix elements and are found to be

$$\langle R_2^h | r_h | R_1^h \rangle \approx \frac{214.4}{a} \tag{B.12}$$

and

$$\langle R_0^h | r_h | R_0^h \rangle \approx \frac{0.5248}{a}. \tag{B.13}$$

Inserting these values into our Stark effect matrix elements yields, for example,

$$\left\langle \psi_{\alpha}\psi_{\frac{3}{2}, \frac{1}{2}}^+ \left| \hat{E} \right| \psi_{\alpha}\psi_{\frac{1}{2}, \frac{1}{2}}^+ \right\rangle \approx (24.79)\frac{eE_0}{a}\langle \psi_{\alpha} | \psi_{\alpha} \rangle, \tag{B.14}$$

which determines an A -coefficient of about 24.79.